Nano Energy 127 (2024) 109799

Contents lists available at ScienceDirect

Nano Energy

journal homepage: www.elsevier.com/locate/nanoen

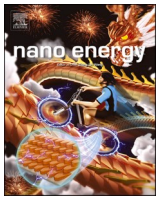

Bioinspired composite fiber aerogel pressure sensor for machine-learning-assisted human activity and gesture recognition

Wenke Yang [a,b], Shun Liu [a,b], Ziqi Wang [a,b], Hu Liu [a,b,*], Caofeng Pan [c], Chuntai Liu [a,b], Changyu Shen [a,b]

[a] State Key Laboratory of Structural Analysis, Optimization and CAE Software for Industrial Equipment, Zhengzhou University, Zhengzhou, Henan 450002, China
[b] National Engineering Research Center for Advanced Polymer Processing Technology, Zhengzhou University, Zhengzhou, Henan 450002, China
[c] Institute of Atomic Manufacturing, Beihang University, Beijing 100191, China

ARTICLE INFO

Keywords:
Polyimide fiber
Conductive composite fiber aerogel
Biomimetic structure
Pressure sensor
Wearable electronic devices
Machine learning

ABSTRACT

Machine-learning-assisted human activity and gesture recognition are valuable for human-computer interaction, and data acquisition often necessitates high-performance sensors. Here, inspired by spider web and bat wing airflow sensing system, polyimide fiber (PIF)/carbon black (CB) composite fiber aerogel (CFA) pressure sensor with biomimetic hair-Merkel cell sensitive unit was developed, exhibiting ultralow detection limit (2 Pa), high pressure sensitivity (S=23.1 kPa^{-1}), wide linear detection capacity up to 67.61 kPa, and fast response/recovery time (140/100 ms). Thanks to the excellent mechanical property and environmental tolerance of CFA, it also possesses excellent low fatigue over >4000 cycles and good durability even at extreme high-temperature (200 °C) and underwater conditions. The superior signal data of the sensor, combined with the Convolutional Neural Network machine learning algorithm, achieves ultra-high prediction accuracies of 96.73% and 98.26% for human activity and gesture recognition, respectively. Additionally, CFA also has amazing thermal management properties, making it to be an ideal candidate for wearable electronics with excellent wearing comfort and safety.

1. Introduction

Accurate recognition of human activity and gestures can enable seamless human-computer interaction for device control and healthcare systems [1–6]. This interaction can be automated using simple and efficient convolutional neural network (CNN) machine learning algorithms to recognize motion models [7–11]. In order to improve identification accuracy, data acquisition usually requires a combination of sensors with excellent performance. Piezoresistive pressure sensors that convert external mechanical compression into resistance sensing signal are currently considered to be the most promising technology owing to their advantages of simple preparation, rich raw materials, and easy signal processing [12–15]. Actually, pressure detection often necessitates the use of pressure sensors with both high sensitivities to minimize the interference from noisy signals and wide linear sensing range to enhance their applicability in different working environments, which is still a great challenge for the design and preparation of high-performance piezoresistive pressure sensors [16,17].

Mechanotransduction is ubiquitous in biological systems, where the bioreceptors often have the typical structures optimized for extremely high sensitivity [18,19]. Thus, introducing the biological structures for the design of pressure sensor turns to be a promising approach to improve the sensing performance, and enormous progress has been achieved in previous research [14,20–23]. Kang et al. mimicked the surface topology of spider's sensory system and constructed an ultrasensitive strain sensor (GF~2000) by introducing a crack structure in a conductive thin film, thus realizing the real-time monitoring of various physiological activities of the human body [24]. Zhou et al. developed a highly sensitive adaptive graphene/single-walled nanotube-Ecoflex membrane (GSEM) airflow sensor with an ultra-low airflow velocity detection limit of 0.0176 m s^{-1}, which is mainly ascribed to the constructed reversible microspring effect inspired by the airflow receptor (hair-Merkel cell) within the bat wing membrane [25]. Additionally, our previous research reported a conductive composite fiber aerogel (CFA) pressure sensor with the spider web-like structure, which is helpful for excellent linear sensing behavior across the entire detection range

* Corresponding author at: State Key Laboratory of Structural Analysis, Optimization and CAE Software for Industrial Equipment, Zhengzhou University, Zhengzhou, Henan 450002, China.
E-mail address: liuhu@zzu.edu.cn (H. Liu).

https://doi.org/10.1016/j.nanoen.2024.109799
Received 3 May 2024; Received in revised form 22 May 2024; Accepted 26 May 2024
Available online 28 May 2024

(0.01–53.34 kPa), and the intrinsic sensing mechanism of the biomimetic structure was also verified through finite element simulation analysis and equivalent circuit model calculations [26].

In this article, we proposed an accurate human activity and gesture recognition system utilizing a high-performance pressure sensor and CNN machine learning algorithms. Specifically, spider web-like conductive polyimide fiber (PIF)/carbon black (CB) composite fiber aerogel (CFA) pressure sensor with biomimetic hair-Merkel cell sensitive unit was prepared, exhibiting decent performances of low detection limit (2 Pa), high pressure sensitivity (23.1 kPa^{-1}), wide linear detection range (up to 67.61 kPa), fast response and recovery time (140/100 ms), and exceptional long-term durability (4000 cycles). With CNN machine learning algorithms assistance, exceptionally high prediction accuracies of 96.73% and 98.26% for human activity and gesture are respectively attained. Notably, due to the phenomenon of "motion spillover," fingers are susceptible to tendon crosstalk in a relatively small number of flexions that results in uncontrolled flexion of adjacent fingers, leading to signal interference between different fingers. Even so, our resultant pressure sensor can still achieve a prediction accuracy of 95.98% for different gestures. In addition, the sensor also possesses great potentials in haptic interfaces, i.e., human-machine interaction, intelligent gripping, and electronic scale. Importantly, owing the excellent applicability in extreme environments and good thermal management capacity of the sensor, our work will undoubtly contribute to the further development of smart wearable devices that can ensure the comfort and safety of the wearer during human activity and gesture recognition.

2. Experimental procedures

2.1. Chemicals and materials

4,4'-Diaminodiphenyl ether (ODA, AR, 98%), 3,3',4,4'-biphenyltetracarboxylic dianhydride (BPDA, AR, 97%) and dioxane (AR, 99%) were purchased from Shanghai Aladdin Biochemical Technology Co., Ltd, China. N-Methyl-2-pyrrolidone (NMP, AR, 97%) and triethylamine (TEA, AR, 99%) were bought from Tianjin Damao Chemical Reagent Factory, China. Electrospun polyimide fibrous film was purchased from Jiangxi Xiancai Nanofibers Technology Co., Ltd, China. Aqueous carbon black (CB) slurry with a concentration of 10 wt% was kindly provided by Zhongshan Runze Nanotechnology Co., Ltd., China. All the chemicals and materials were used directly as received without further treatment.

2.2. Fabrication procedure

2.2.1. Synthesis of PAA

PAA was synthesized according to the following typical procedure. Firstly, 2 g of ODA and 2.94 g of BPDA were added to 25 mL of NMP and reacted under mechanical stirring at 0°C for 10 h. After that, 1.4 mL of TEA was added and stirred vigorously for 2 h, and the resultant light yellow viscous PAA solution (~13.84 wt%) was then poured into 600 mL of deionized (DI) water with vigorous stirring for solvent replacement. Finally, the generated precipitate was repeatedly suction filtered and washed using DI water for several times, and then freeze-dried (10 Pa, -80 °C, 72 h) to obtain the water-soluble white PAA powder (Figure S1).

2.2.2. Preparation of PIF

Commercial electrospun polyimide fibrous film was first cut into small pieces and soaked in dioxane overnight. Afterwards, the above mixture was treated by a high-speed shear homogenizer (FJ200-SH) at a speed of 13000 rpm for 25 minutes to segment the film into short fibers, which was then frozen in refrigerator (-20 ℃) overnight and freeze-dried (5 Pa, -80 °C) for 72 h to obtain the fluffy PIF with an average length of ~350 nm (Figure S2).

2.2.3. Preparation of conductive composite fiber aerogel

Typically, 50 mg of PAA was first dissolved in 20 mL of TEA aqueous solution (5 vol%) under stirring for 20 min, and then 100 mg of PIF and 400 μL of aqueous conductive CB slurry were subsequently added and stirred for another 50 min to obtain the homogenous PAA/PIF/CB mixture. After that, the mixture was transferred to the desired mold, frozen in refrigerator (- 20 ℃) overnight, and freeze-dried (5 Pa, -80 °C) for 72 h, obtaining the PAA/PIF/CB aerogel. Finally, thermal imidization treatment (350 ℃, 1 h) was conducted in nitrogen atmosphere to achieve the transformation of PAA into PI, obtaining the designed conductive PIF/CB composite fiber aerogel (CFA). In addition, as shown in Table S1, series of PIF/CB CFAs with different CB content were also prepared using the same procedure, and the prepared sample was named as PIF/CB-x, where x refers to the mass ratio of CB and PIF.

2.3. Characterizations

Scanning electron microscope (SEM) images were taken by a JEOL JSM-7500 F instrument at an accelerating voltage of 5 kV. Dynamic mechanical analysis (DMA) was performed by a dynamic thermo-mechanical analyzer (TA Q800) at a heating rate of 5°C min^{-1} in the temperature range of -50–300 °C with a set frequency of 1 Hz and a fixed oscillating strain of 2%. Compression mechanical properties were tested using a universal testing machine (UTM2203) equipped with a 100 N sensor. The real-time electrical signal was collected by the electrochemical workstation (CHI660, Shanghai Chenhua). Multi-channel electrical signals were collected by a portable Bluetooth wireless transmission resistance measurement device (TruEbox 01RC, LinkZill). Thermal insulation property of sample was tested by placing the CFA on the frozen copper block (-20℃) and on the hot stage (ANSAI 946 C) set at different temperatures (Figure S3). Solar simulator (CEL-PE300L–3A, Beijing China Education Au-light CO., Ltd.) was used to irradiate the CFA to test its photothermal conversion performance, and the optical power density was achieved by adjusting the distance between the sample and the light source. Infrared thermal images and the real-time temperature during the thermal insulation and photothermal conversion tests were recorded using an infrared camera (FLIR E8). In this work, PIF/CB-0.4 CFA was selected for all the tests unless otherwise stated.

3. Results and discussion

In nature, most organisms have very sensitive sensory systems and can respond quickly and effectively to external stimuli [27,28]. The bat is the only mammal that can fly at high speed owing to its wings that are ultra-sensitive to air currents. As seen in Fig. 1a, bat wing is distributed with a large number of ultra-sensitive airflow sensing organs composed of body hairs and Merkel cells. Specificality, for the bat flight, air currents flow over the wings, leading to the reversible mechanical bending displacements of the hairs distributed across the wing surface. As a result, the Merkel cells located around the hair follicles can be rapidly stimulated, generating the corresponding cellular action currents, which transmit to the central nervous system via nerve fibers to provide real-time airflow sensing [25,29,30]. Inspired by the special structure of bat wing, we designed a biomimetic CFA composed of polyimide fiber and CB particle that act as the body hair and Merkel cell to construct the pressure-sensitive unit, where the pressure induced deformation of fiber can effectively change the CB conductive network, generating high-efficient pressure sensing signal. Here, the simple solution blending and freeze-drying technique was applied for the preparation of PIF/CB CFA, Fig. 1b. In details, water soluble PAA powder and PIF were first homogeneously dispersed into ultrapure water with the assistance of TEA (Figure S4), then CB slurry was added and mixed evenly to obtain the stable and homogeneous PIF/PAA/CB dispersion (Figure S5). After being completely frozen in the desired mold, PIF/PAA/CB were fully trapped between ice crystals, which were then freeze-dried and

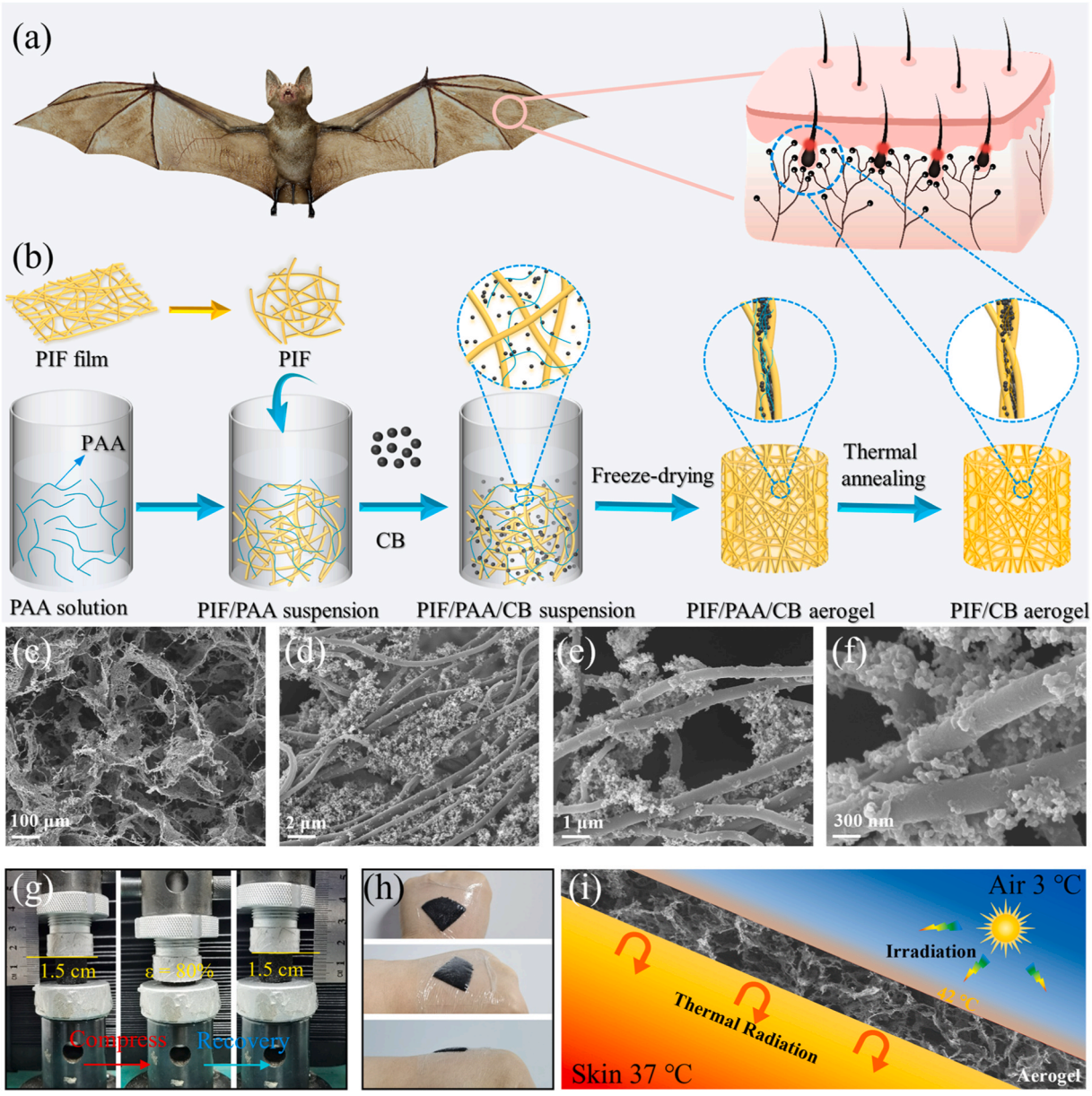

Fig. 1. Concept and design of a bat-wing inspired conductive CFA. (a) Brief structure of bat wing, whose keen perception comes from the stimulation of Merkel cells caused by body hair deformation. (b) Preparation process of PIF/CB CFA and the biomimetic hair-Merkel cell pressure-sensitive unit. (c-f) SEM images of PIF/CB CFA with different magnifications. (g) Excellent compressibility and resilience of PIF/CB CFA even under 80% compression strain. (h) Perfect adaptability of PIF/CB CFA on body skin. (i) Schematic diagram of PIF/CB CFA with excellent human thermal management performance.

sublimated to obtain the PIF/PAA/CB CFA. Subsequently, a typical thermal annealing was conducted to achieve the conversion of PAA to PI via the dehydration and cyclization in PAA, obtaining the final PIF/CB CFA. Here, the polymeric PI acted as the "glue" to ensure a strong PIF-PIF and PIF-CB interfacial interactions, constructing the robust cellular skeleton and efficient conductive network. Additionally, it should be noted that our previous work has proved that the added TEA can be completely removed during this process without affecting the mechanical property of PIF [26].

Fig. 1c displays the microstructure of the prepared PIF/CB CFA, where the typical isotropic three-dimensional open-cellular structure with a pore size of 150 μm can be clearly observed. Zooming in on a cellular wall reveals a spider web-like network formed by overlapping and entangling of PIF (Fig. 1d&e) and the CB particles are anchored on the fiber surface (Fig. 1f), constructing the effective conductive networks and special biomimetic hair-Merkel pressure-sensitive unit. Similar to ultra-sensitive airflow sensing mechanism of batwing, squeezing and bending of the interlacing PIF upon external pressure can easily lead to contact of adjacent anchored CB particles that generates significant resistance variation, providing the biomimetic PIF/CB CFA with ultrasensitive pressure sensing capacity. Due to the good bonding function of polymeric PI and hierarchical fibrous porous structure, as shown in Fig. 1g, the prepared PIF/CB CFA can withstand an 80% compression strain and recover to its original height after releasing the compression, showing excellent mechanical compressibility and resilience, which is critical for a robust and stable pressure sensor. In addition, PIF/CB CFA also has excellent flexibility, allowing for good conformal contact with human skin (Fig. 1h). Furthermore, due to the unique ultra-high porosity structure of aerogel as well as the excellent photo-heating capability of CB, the designed biomimetic PIF/CB CFA can also be endowed with excellent human thermal management capacity (Fig. 1i). All these outstanding merits stated above will undoubtly

make it to be an excellent candidate for future wearable smart devices with great wearing comfort.

Compression mechanical properties of PIF/CB CFA, including strength, modulus, elasticity, and fatigue resistance, are the critical factors that affect its suitability for pressure sensor and overall pressure sensing performances. Here, the effect of CB content on the mechanical properties of PIF/CB CFA was first investigated. As shown in Figure S6 and Fig. 2a, significant enhancement in mechanical property is obviously observed with increasing CB content, and the compression strength (which refers to the stress at the 50% strain) and modulus of PIF/CB-0.6 CFA reaches 12.34 kPa and 8.67 kPa, respectively, which is 240% and 570% higher than that of PIF/CB-0.2. Such an enhancement can be ascribed to the excellent mechanical property of PI, robust hierarchical fibrous porous structure, and good interfacial interaction between PIF and CB with the help of polymeric PI that ensure the effective stress transfer upon external compression. Notably, compared with our previous works, the low modulus characteristic of PIF based composite aerogel is well kept for all the PIF/CB CFA, which is an important prerequisite for highly pressure sensitive capacity. Additionally, as seen in Fig. 2b, the conductivity of PIF/CB CFA also increases with the increase of CB content, which is mainly attributed to the gradual increase of CB particles anchored on fiber surface that results in a more perfect conductive network, but this can also affect the designed biomimetic hair-Merkel structure and pressure sensing performance which will be discussed in the following part. Furthermore, it is well known that the collapse of cellular skeleton caused by the sublimation of ice crystal during the freeze-drying process and the contraction of fiber induced by the dehydration and cyclization of PAA during the thermal annealing process can usually lead to obvious shrinkage of aerogel. As for the resultant PIF/CB CFA, it can be clearly observed from Fig. 2c that the shrinkage can be effectively restrained with increasing CB content owing to the supporting effect of CB particles, and the shrinkage rate is significantly reduced to 0% for PIF/CB-0.4 CFA and the one with higher CB content. Meanwhile, the density exhibits an increasing trend, and the porosity displays a decreasing trend especially for the PIF/CB CFA with a higher CB content, which will undoubtly affect the fibrous cellular structure and lightweight merit of aerogel to some extent. Therefore, it is expected that the application requirements for PIF/CB CFA with different characteristics can be well fulfilled via tunning CB content.

Fig. 2d exhibits the cyclic compression curves of PIF/CB CFA under stepwise cyclic compression, and the typical hysteresis loop of compressible elastic foam is clearly observed for different strain, showing the elastic fibrous cellular structure of the aerogel. During the compression process, the stress increases linearly within 0–50% strain (linear elastic region) owing to the elastic deformation of the fibrous cellular skeleton, then it displays a sharp increase with the increase of

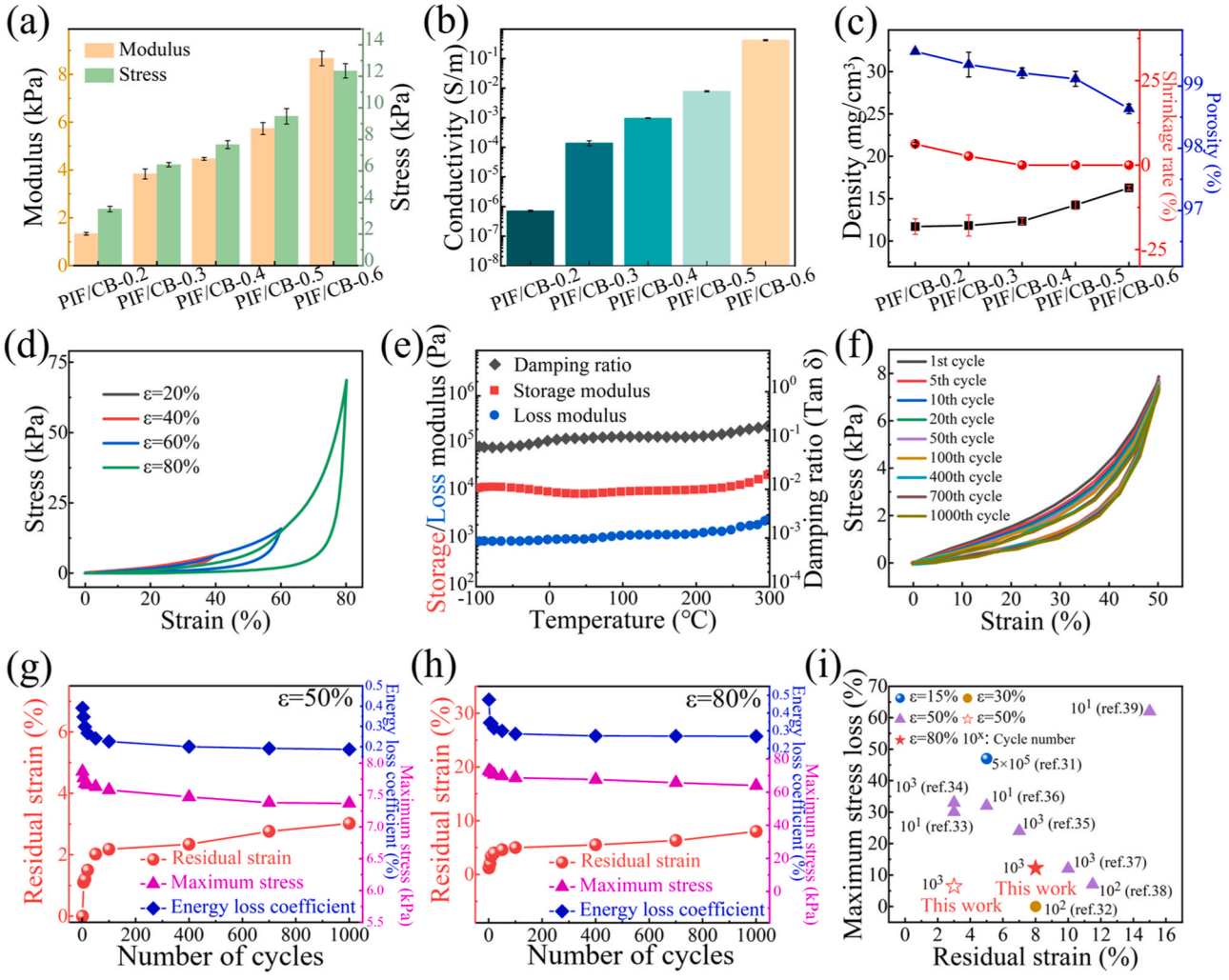

Fig. 2. Compression mechanical properties of PIF/CB CFA. (a) Compressive strength and modulus, (b) conductivity and (c) density, porosity, shrinkage rate of different PIF/CB CFA. (d) Stress-strain curves of PIF/CB CFA under stepwise cyclic compression. (e) Dynamic compressive viscoelastic property of PIF/CB CFA. (f) Stress-strain curves of PIF/CB CFA over 1000 cycles at 50% strain. Statistics of the residual strain, maximum stress, and energy loss coefficient of PIF/CB CFA over 1000 cycles at (g) 50% strain and (h) 80% strain. (i) Maximum stress loss and residual strain of PIF/CB CFA compared with other reported aerogel materials.

strain to 80% (densification region) arising from the contraction of porous structure. Besides, dynamic mechanical analysis of PIF/CB CFA over a temperature range of -100–300°C was also conducted (Fig. 2e), the almost invariant viscoelastic properties (storage modulus and loss modulus) indicate the excellent tolerance to extreme temperature, and the small damping ratio of 0.1 illustrates the little energy loss that is beneficial for outstanding elasticity. All these will undoubtly enable it to be applicable for stable pressure detection over a wide strain and temperature range. Fatigue resistance of PIF/CB CFA over 1000 cycles at 50% strain was then further studied, and the typical hysteresis loops are almost coincided with each other especially for the larger cycle number (Fig. 2f). As seen in Fig. 2g, maximum stress, energy loss coefficient, and residual strain exhibit a significant variation in the initial 20 cycles owing to the destruction and rearrangement of the unstable cellular structure, then they tend to be stable based on the newly reconstructed stable three-dimensional cellular structure. Specifically, the maximum stress is reduced by 6.3% (from 7.87 kPa to 7.37 kPa) and the residual strain is only 3% for the 1000th cycle, indicating the excellent fatigue resistance arising from the robust and superelastic biomimetic fibrous cellular structure. What's more, PIF/CB CFA also exhibits the similar fatigue resistance towards a larger strain of 80% (Figure S7&2 h). According to the comparation results with other reported aerogel materials shown in Fig. 2i, our prepared PIF/CB CFA possesses a significant competitive advantage in both maximum stress loss and residual strain at both 50% and 80% strain [31–39]. As a result, the good comprehensive mechanical properties of PIF/CB CFA, including outstanding elasticity, robustness, and fatigue resistance, make it to be an excellent candidate for high-performance pressure sensor.

Pressure sensing performance of PIF/CB CFA under unidirectional compression was first systematically investigated. Fig. 3a records the real-time relative current variation ($\Delta I/I_0=(I-I_0)/I_0$, where I and I_0 represent the instantaneous current and initial current, respectively) with increasing compression strain, where the $\Delta I/I_0$ increases linearly and slowly in the initial strain range of 0–30%, generating a strain

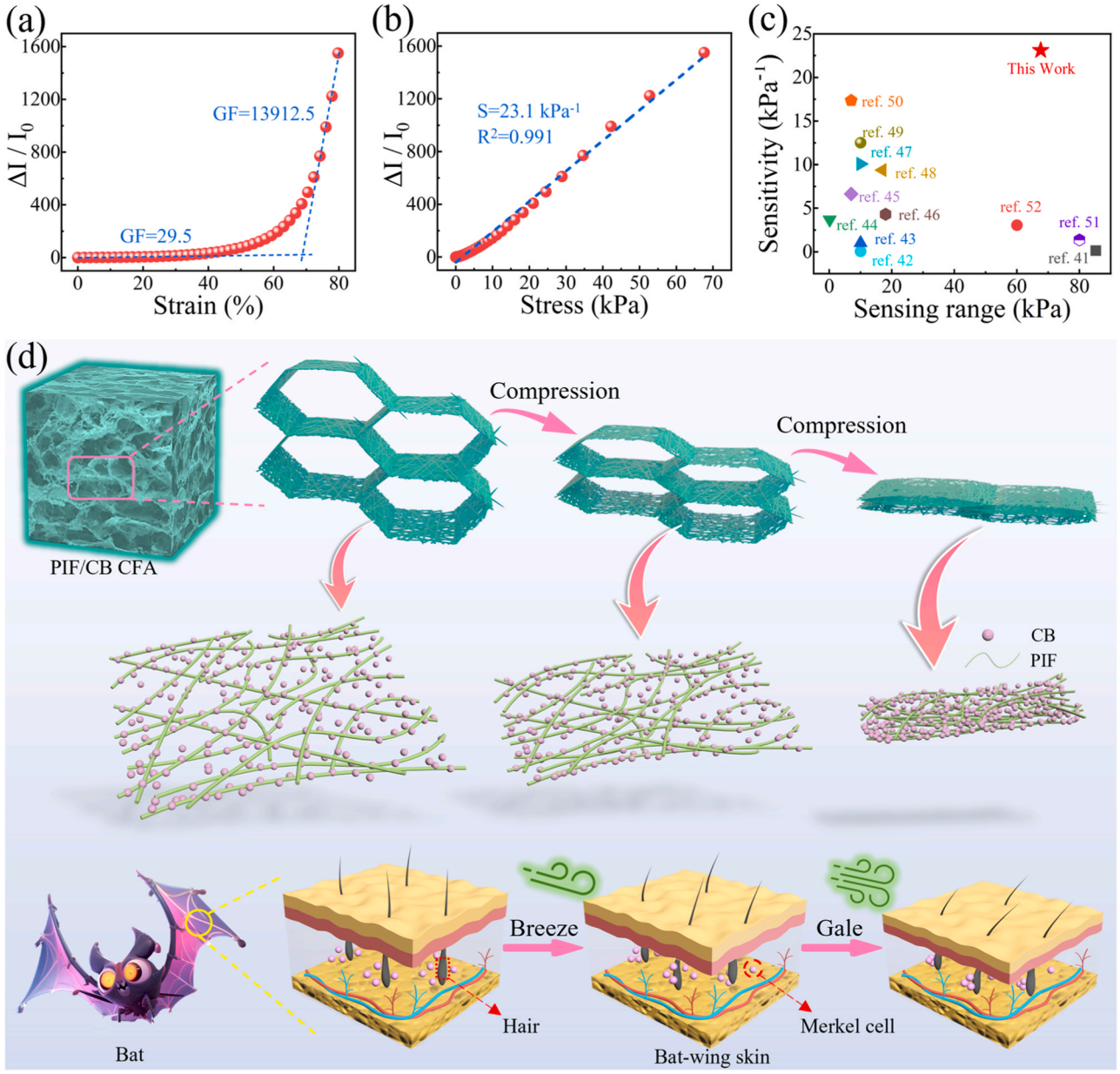

Fig. 3. Pressure sensing performance and mechanism analysis of PIF/CB CFA. Relative current variation versus (a) strain and (b) pressure of PIF/CB-0.4 CFA upon external compression. (c) Comparation of the sensitivity and sensing range of our prepared biomimetic PIF/CB CFA with other reported pressure sensors. (d) Schematic of pressure sensing mechanism of the biomimetic PIF/CB CFA, which is well corresponded with the wind speed perception mechanism of bat wing.

sensitivity (Gauge Factor, GF= $(\Delta I/I_0)/\varepsilon$, where ε stands for the applied strain) of 29.5 that is still much higher than other our previous PIF based pressure sensor [26,40,41]. After that, it exhibits an exponential growth trend followed by a sharp increase for the strain higher than 70%, and an ultrahigh strain sensitivity up to 13912.5 is obtained. As shown in Fig. 3d, the excellent strain sensitivity is closely related with the spider web-like cellular skeleton of CFA, which is composed of the typical biomimetic hair (PIF)-Merkel cell (CB) sensitive unit of bat wing. So, the pressure working mechanism of the CFA is similar to wind speed perception mechanism of the ultrasensitive airflow detection organs of bat wing, of which the deformation of body hairs and compression of skin under various surrounding air turbulence can effectively trigger the Merkel cells to sense complex airflow change for smooth flight, and more Merkel cells can be effectively stimulated upon a higher flight speed. When the aerogel undergoes a small compression within the elastic range (<30%), the fibrous cellular skeleton is subjected to a significant squeeze that leads to the bending deformation of overlapped PIFs, triggering the adjacent separated CB particles anchored on the surface to contact with each other. Such a typical "point-point" connection is critical for the significant increase of effective conductive networks, resulting in the biomimetic sensing behavior with a high strain sensitivity. With further compression, the densification of the cellular structure gradually occurs, where the bending deformation of PIF turns to be more serious and the adjacent cellular wall also begin to contact, so the biomimetic sensing mechanism turn to be stronger that enables a much higher sensitivity.

Meanwhile, according to the stress-strain curve of PIF/CB CFA (Figure S8), pressure sensitivity ($S=(\Delta I/I_0)/P$, where P denotes the applied pressure) was also studied and shown in Fig. 3b. It can be clearly seen that $\Delta I/I_0$ varies linearly within a wide pressure range of 0.002–67.61 kPa and a stable ultrahigh pressure sensitivity of 23.1 kPa^{-1} is acquired, which is mainly ascribed to the low compression modulus of PIF/CB CFA that enables the significant deformation of fibrous cellular skeleton and the fibrous porous structure upon small pressure variation, generating the designed biomimetic ultrasensitive sensing capacity. Additionally, the linear sensing behavior can be attributed to the fibrous porous structure which has been well explained in our previous work [26]. Meanwhile, owing to the CB content dependent microstructure of CFA, the pressure sensing performance of CFA with various CB content was also systematically investigated to further emphasize the

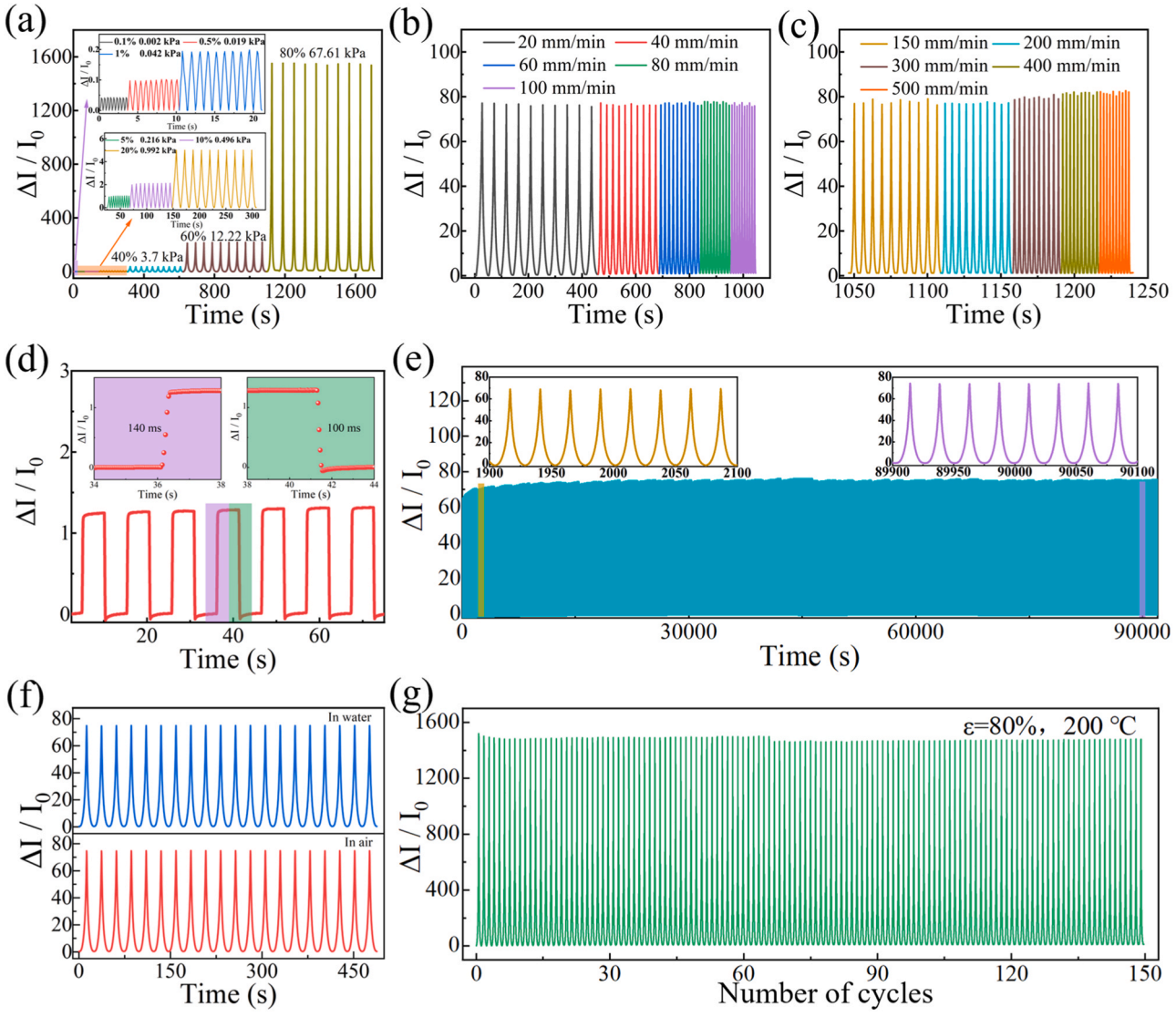

Fig. 4. Pressure sensing performances of PIF/CB CFA. Cyclic response curves of PIF/CB CFA under (a) different strains/stress (20 mm/min) and (b&c) different compression rates under 50% strain. (d) Response/recovery time of PIF/CB CFA at a compression rate of 500 mm/min under 5% strain. (e) Long-term durability of PIF/CB CFA over 4000 cycles at a compression rate of 20 mm/min under 50% strain. Sensing stability of PIF/CB CFA (f) in water environments (ε=50%, 20 mm/min) and (g) over 150 cycles under extreme working conditions (ε=80%, 200 ℃).

importance of biomimetic sensing unit. As seen in Figure S9a&b, compared with the CFA discussed above, non-linear sensing behavior with a lower sensitivity especially in the low-pressure region was observed for the CFA with lower CB content, which is mainly due to the insufficient CB that hinders the construction of effective conductive fibrous structure and the designed biomimetic hair (PIF)-Merkel cell (CB) sensitive unit, exhibiting the unsatisfied pressure sensing performance. As for the CFA with higher CB content (Figure S9c&d), the pressure sensitivity shows a decreased trend and the linear sensing pattern also gradually disappears, which can be explained by the fact that excessive CB particles tend to aggregate around PIF and fill the gap between the adjacent overlapped PIFs, destroying the typical biomimetic sensitive unit and conductive fibrous structure to some extent. Thus, as shown in Fig. 3c, our prepared PIF/CB CFA with a proper CB content is critical for the achievement of both high sensitivity and wide linear response range, showing a competitive advantage over the latest reported literatures [41–52].

Subsequently, pressure sensing performances of PIF/CB CFA pressure sensor were systematically investigated. Fig. 4a depicts the sensing pattern of the sensor upon cyclic compression to different strain/stress levels, where the $\Delta I/I_0$ exhibits stable and repeatable change upon periodic compression and releasing, and the response peak shows an increasing trend with increasing strain/stress up to 80% strain (67.61 kPa). Hence, different pressure levels can be accurately identified according to the stable electrical sensing signal. Notably, benefiting from the superiority of the bioinspired structure, the sensor can also effectively response to the pressure as low as 0.002 kPa (0.1% strain), enabling it possible to use it to recognize small pressures. When exerting the sensor with series of compression rates under 50% strain (Fig. 4b&c), it can also output stable and reproducible sensing pattern, and the response peak value keeps constant without being affected even at a high-speed of 500 mm/min. Such a typical rate independent pressure sensing behavior allow it to work steadily in various operation conditions without losing detection accuracy. Fig. 4d shows the sensing behavior of the sensor at an ultrahigh compression rate of 500 mm/min under 5% strain, exhibiting a fast response time of 140 ms and recovery time of 100 ms, which is critical for the timely response to external pressure stimulus. Additionally, as illustrated in Fig. 4e, long-term durability and stability of the sensor under 50% strain over 4000 compression cycles were evaluated. Clearly, the sensor displays a stable periodic sensing pattern without obvious fluctuation after a slight increase trend arising from the irreversible residual strain, and the current response peak value keeps constant in both the early and later stages (inserts in Fig. 4e), demonstrating the excellent fatigue resistance of the sensor with negligible sensing signal attenuation. Thanks to the low surface energy of PI, rough CB particles anchored fibrous cellular skeleton, and porous structure of aerogel, the resultant PIF/CB CFA pressure sensor possesses excellent hydrophobicity. As a result, the sensor has the same pressure sensing capacity in water as that in air (Fig. 4f&S10), demonstrating the great application potential in underwater detection. In addition, most polymer-based pressure sensors can usually lose their sensing capacity under high temperature environment due to the pyrolysis of polymer matrix, so the usage of excellent high temperature tolerant PI can be an effective strategy. As seen in Fig. 4g, pressure sensing performances of the PIF/CB CFA pressure sensor under 80% strain was performed at a high temperature of 200 °C, and the expected outstanding stable sensing behavior without significant reduction is clearly observed, which is expected to be applied to extreme environments such as outer space exploration and high-temperature workshops. The above results demonstrate that the PIF/CB CFA is a high-performance pressure sensor capable of withstanding high temperatures, high humidity, and high pressure, which is very valuable for practical applications.

Owing to the excellent mechanical properties, high sensitivity, and wide sensing range of our prepared PIF/CB CFA pressure sensor, it possesses great potential in wearable electronic device for real-time human physiological and motion monitoring. Fig. 5a shows the periodic pulse sensing signal of the sensor attached to the wrist, and the pulse rate is calculated to be ~60 beats per minute, which is well within the normal value of healthy people. Meanwhile, the typical characteristic peaks of "P" (percussion wave), "T" (tidal wave), and "D" (diastolic wave) of the pulse waveform are also clearly identified from the enlarged view shown in Figure S11, which can be attributed to the high sensitivity and ultralow detection limit of the sensor. Additionally, the sensor fixed onto the cheek can also output regular sensing signal towards the facial micro-expressions, and the smile and laugh can be easily recognized based on the response intensity induced by the different facial muscle contraction degree (Fig. 5b). Furthermore, the sensor was also applied for the detection of joint activity, where the sensor outputs stable and reproducible response pattern to the repeated finger bending (Fig. 5c), elbow bending (Fig. 5d), and knee bending (Fig. 5e), indicating the good recognition capacity for vigorous human activities. Notably, it can accurately identify the finger bending frequency based on the response peak number within a certain period (Fig. 5c) and distinguish the specific body joint according to the response peak shape (Fig. 5d&e). All these will undoubtly make it to available for the smart wearable applications in personal lifecare and healthcare services for the elderly and disabled people. In order to facilitate human-computer interaction and enable large-scale applications of sensors, a machine learning algorithm based on convolutional neural networks (CNN) has been designed to train and recognize data from human activity signals. After acquiring and preprocessing the data, we obtained 200 distinct sets of human activity data, of which 80% was used to train the model and the remaining 20% was reserved for testing its performance (Fig. 5f). The dataset of electrical signals from various activities was validated using a CNN classification algorithm for training and testing, resulting in a confusion matrix displayed in Fig. 5g with a prediction accuracy of 96.73%. In addition, the prediction performance can be further improved by adding training data. These results demonstrate the ability of PIF/CB CFA to accurately recognize different human activities.

Furthermore, the prepared pressure sensors were fixed onto the joints of the five fingers with the help of medical tape for gesture recognition (Fig. 5h). When the volunteer makes a specific gesture, the assembled five sensors output a set of sensing signals which is well corresponded with the finger bending state (Fig. 5i&S12). Benefiting from the excellent comprehensive properties of the biomimetic PIF/CB CFA, the sensor still shows outstanding low noise under the complex deformation of finger joints and can accurately recognize various gestures. Therefore, a CNN machine learning algorithm was used to evaluate the capability of PIF/CB CFA in recognizing various gestures. As shown in Fig. 5j, the prediction accuracy of PIF/CB CFA for different consecutively made gestures can reach up to 95.98%, which is a good indication of its ability to accurately recognize various gestures. Notably, “motor overflow” can cause crosstalk between the tendons of different fingers, resulting in uncontrolled flexion of the adjacent fingers during a relatively minor flexions of one finger, but this phenomenon diminishes after several repetitions of flexion. Therefore, making different gestures consecutively leads to crosstalk of the signals thus exhibiting relatively low training accuracy. Based on this, the same cycle number of data acquisition were performed for each gesture, and it can be observed that the sensor exhibits a stable cyclic sensing signal (Fig. 5k&l). The obtained data is then trained and tested using the CNN machine learning algorithm, and the amount of data used is kept the same as in Fig. 5i for comparison purposes. The results show that the recognition accuracy of PIF/CB CFA for different gestures is enhanced to 98.26% after eliminating the crosstalk of the motion overflow phenomenon (Fig. 5m). All these show that PIF/CB CFA has amazing application prospects for gesture recognition. In addition, in future scenarios, PIF/CB CFA can be applied to human-computer interaction applications in virtual reality as well as the operation of remote-controlled manipulators such as tele-surgery, disaster relief, and industrial robots through smart terminals.

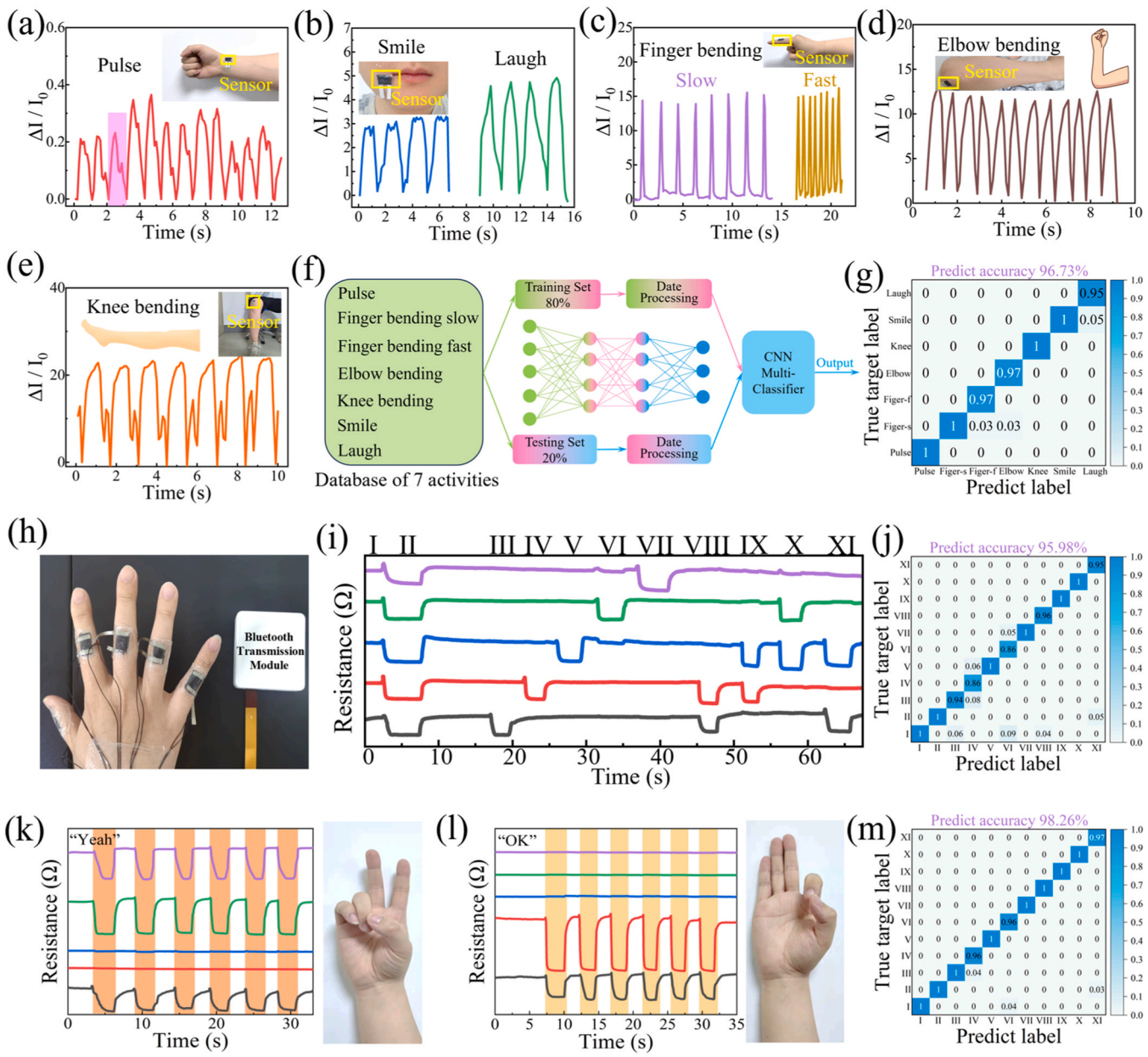

Fig. 5. Machine learning assisted PIF/CB CFA pressure sensors for highly accurate human activity and gesture recognition. (a) Real-time current signals of the sensor responding to pulse, (b) facial micro-expressions, and various human motions including (c) finger, (d) elbow, and (e) knee bending. (f) Flowchart of machine learning algorithm for human activity based on convolutional neural network (CNN). (g) Confusion matrix for validating the results of human activity classification. (h) Digital photograph showing the assembled gesture recognition system. (i) Multichannel electrical signal responses to 11 commonly used gestures made in succession. (j) Confusion matrix for validating the recognition results of 11 different consecutive gestures. (k&l) Cyclic stability of specific gestures. (m) Confusion matrix for validating the recognition results of two specific gestures.

As for the tactile sensing applications of the resultant PIF/CB CFA pressure sensor, flexible electronic skin consisting of 4 × 4 sensing array was first assembled for spatial pressure distribution detection, and each sensing unit is composed of the mutually non-interfering interdigital electrodes and pressure sensor. When placing a toy cat and different balance weights on the surface of electric skin respectively (Fig. 6a&b), the contacting sensing unit will output the specific electrical response signal based on the corresponding pressure. As seen in Fig. 6a'&b', three-dimensional current change mapping of the sensor array is clearly collected, which is well consistent with the location, shape and weight of the placed item, demonstrating the accurate recognition ability of the resultant electronic skin. Besides, as illustrated in Fig. 6c, the pressure sensor was attached onto the fingertip for real time grasping force monitoring. Obviously, both the sensor of index finger and thumb finger display a weaker electrical response signal when grasping less magnet blocks (Fig. 6d), manifesting a lower grasping force. This will undoubtly make it available for the bionics tactile sensor of robotic hand, which is essential for the precise and safe mechanical grasping operation of robotic manipulator. What's more, a facile electronic scale was assembled via coupling the pressure sensor with a portable Bluetooth signal transmission device (Fig. 6e). As expected, the sensor outputs stable electrical response signal rapidly towards different specifications of balance weights (50 g, 100 g, 200 g), and stronger response peak is obtained for a heavier one (Figure S13). Importantly, as seen in Fig. 6f, the calculated resistance variation ΔR has a good linear relationship with different specifications of balance weights, enabling it to assessment the practical weight of different items accurately.

Wearable electronic devices not only require excellent sensing

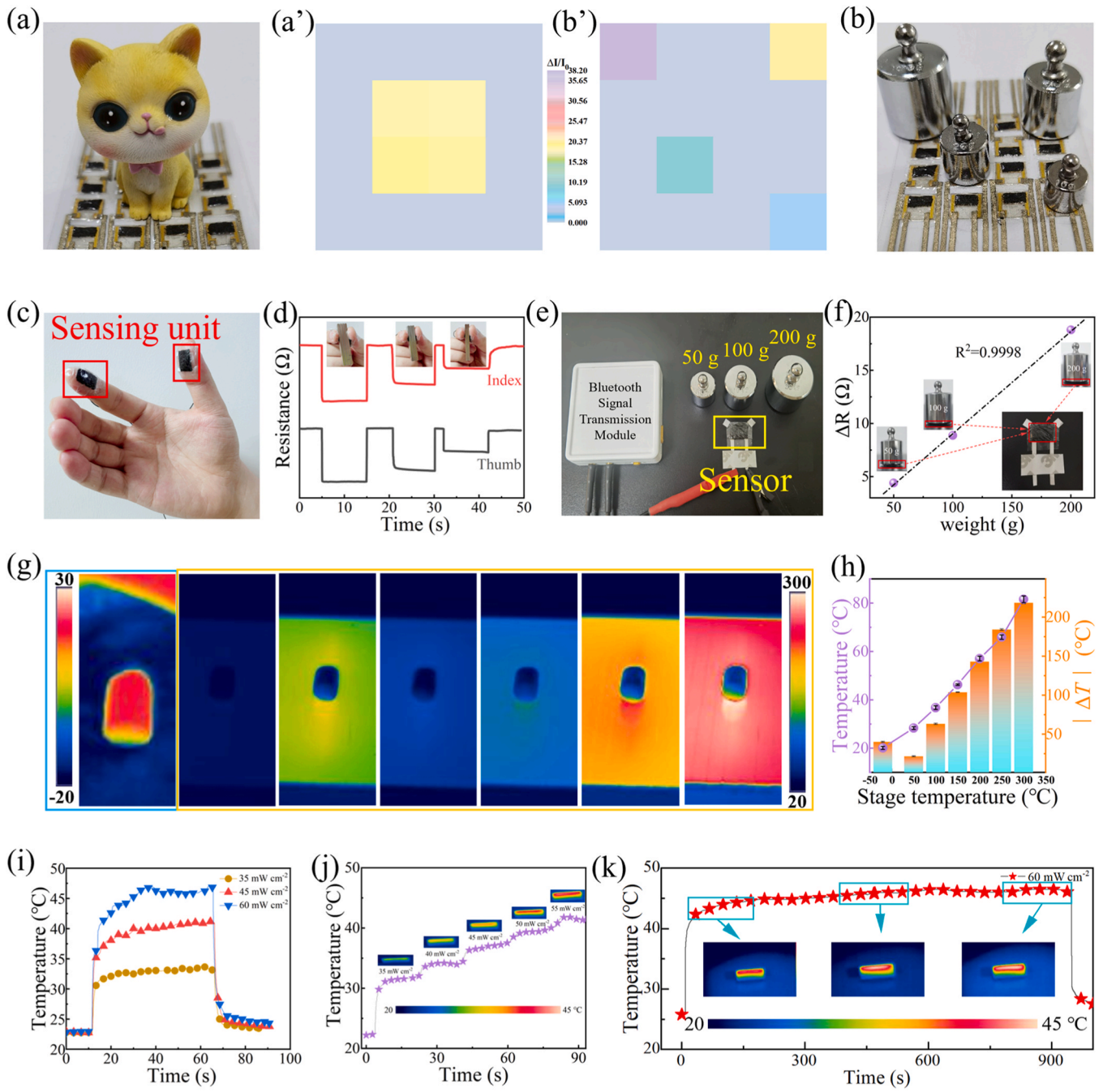

Fig. 6. Evaluation of PIF/CB CFA pressure sensor for tactile sensing applications and human thermal management. Assembled electric skin consisting of 4 × 4 pressure sensor array for spatial pressure distribution detection of (a) toy cat and (b) disorderly distributed balance weights, and (a'&b') their corresponding three-dimensional current change mapping. (c) Grasping force monitoring to the objects with different weights using the pressure sensor fixed onto the fingertip and (d) their corresponding output electric signal. The inset shows digital photos of grabbing objects of different weights. (e) The pressure is connected with a wireless resistance measurement device to simulate a piezoresistive electronic scale. (f) The linear relationship between electrical signal change and weight of balance weights. (g) Infrared thermal images of CFA placed on stages of different temperatures after 30 minutes. (h) The statistical surface temperature of CFA and its temperature difference with the stage. (i) Photothermal conversion curves of CFA under different simulated light power densities. (j) Temperature curve of CFA under stepwise increasing light power density. (k) Photothermal conversion stability of CFA within 15 minutes.

performance, but the good thermal management performance is also indispensable because of the direct interaction with human body. Generally, aerogel is a kind of high-efficient thermal insulation material due to its ultra-high porosity, where the internal amounts of air can significantly reduce the thermal conductivity and the cellular structure is also beneficial for the suppression of thermal convection. When placing the PIF/CB CFA onto the stages of different temperatures (-20−300 ℃) for 30 minutes, it can be seen clearly from the infrared thermal images in Fig. 6g that the CFA exhibits a distinct color difference with the stage, and the color distribution on the surface is almost identical except the boundary area, indicating the excellent thermal insulation property in a wide temperature range. In detail, as displayed in Fig. 6h, the surface temperature of CFA increases slightly with increasing the stage temperature, but a higher surface temperature difference with the stage (ΔT) is obtained for the colder and hotter stage than environment temperature, and ΔT can even reach 220 ℃ in an

environment of 300 °C, improving the wearing comfort and safety of the pressure sensor in both cold and hot environments. Additionally, owing to the excellent optical absorbing ability of CB, exploring the photothermal conversion properties of PIF/CB CFA is of great value for the multifunctional expansion of wearable sensors [53]. As shown in Fig. 6i, the CFA temperature increases sharply after being irradiated and then tends to be stable quickly. Meanwhile, a higher equilibrium temperature is obtained under a stronger light intensity, ensuring the controllable heating performance. Fig. 6j shows the photothermal conversion curve of PIF/CB CFA with stepwise increasing light density, and the CFA temperature presents a fast switching which can be clearly observed from the infrared thermal images (inserts in Fig. 6j), showing a sensitive photothermal response. Moreover, the PIF/CB CFA also shows a stable photothermal conversion ability, and the equilibrium temperature maintains at about 45 ℃ over a period of 15 minutes under a light intensity of 60 mW cm^{-2} (Fig. 6k), demonstrating a steady photothermal conversion efficiency. What's more, piezoresistive pressure sensors can often experience a potential heat accumulation effect during the operation process, which is detrimental in wearable electronic devices as it can cause harm to both delicate electronic components and the human body. Figure S14&S15 show the temperature change of PIF/CB CFA during the cyclic compression process at the working voltage of 1 V, and it can be seen that the sample temperature keeps almost constant much during compression, showing the negligible heat accumulation effect which is favorable for wearable pressure sensors. All these indicate the outstanding human thermal management performance of the PIF/CB CFA pressure sensor, endowing it with great wearing comfort and safety.

4. Conclusion

In summary, we have reported a human activity and gesture recognition system with ultra-high prediction accuracies of 96.73% and 98.26% using the CNN machine learning algorithm assisted CFA pressure sensor. Inspired by spider web and bat wing airflow sensing systems, PIF/CB CFA pressure sensor with biomimetic hair-Merkel cell sensitive unit was prepared, exhibiting ultralow detection limit of 2 Pa, high pressure sensitivity of 23.1 kPa^{-1}, wide linear detection capacity up to 67.61 kPa, fast response/recovery time (140/100 ms), and excellent long-term durability of over 4000 cycles. Our work has also demonstrated that the sensor has the capability for haptic interfaces, such as human-computer interaction, smart grips, and electronic scales, as well as good applicability in extreme environments. Furthermore, our fabricated PIF/CB CFA also has excellent thermal management characteristics, ensuring excellent wearing comfort and safety. We believe this work will undoubtly contribute to the further development of high-precision smart wearables.

CRediT authorship contribution statement

Wenke Yang: Writing – original draft, Visualization, Investigation, Formal analysis, Data curation. **Shun Liu:** Software, Formal analysis. **Ziqi Wang:** Validation, Investigation, Formal analysis. **Hu Liu:** Writing – review & editing, Supervision, Resources, Methodology, Funding acquisition, Conceptualization. **Caofeng Pan:** Writing – review & editing, Methodology. **Chuntai Liu:** Writing – review & editing, Methodology, Funding acquisition. **Changyu Shen:** Funding acquisition.

Declaration of Competing Interest

The authors declare that they have no known competing financial interests or personal relationships that could have appeared to influence the work reported in this paper.

Data Availability

Data will be made available on request.

Acknowledgments

The research was financially supported by National Natural Science Foundation of China (NO: 52373093, 12072325), Outstanding Youth Fund of Henan Province (242300421062), National Key R&D Program of China (2019YFA0706802) and the 111 project (D18023). Informed signed consent was obtained from the volunteer for the human bodily motion and human physical signal detection experiments.

Appendix A. Supporting information

Supplementary data associated with this article can be found in the online version at doi:10.1016/j.nanoen.2024.109799.

References

[1] D. Lee, H. Lee, Y. Jeong, Y. Ahn, G. Nam, Y. Lee, Adv. Mater. 28 (2016) 9364–9369, https://doi.org/10.1002/adma.201603526.
[2] T. Yokota, T. Nakamura, H. Kato, M. Mochizuki, M. Tada, M. Uchida, S. Lee, M. Koizumi, W. Yukita, A. Takimoto, T. Someya, Nat. Electron. 3 (2020) 113–121, https://doi.org/10.1038/s41928-019-0354-7.
[3] M. Amjadi, K.-U. Kyung, I. Park, M. Sitti, Adv. Funct. Mater. 26 (2016) 1678–1698, https://doi.org/10.1002/adfm.201504755.
[4] P. Fratzl, Nature 516 (2014) 178–179, https://doi.org/10.1038/516178a.
[5] K.R.B. Singh, V. Nayak, J. Singh, R.P. Singh, Mater. Lett. 304 (2021) 130614, https://doi.org/10.1016/j.matlet.2021.130614.
[6] D. Verma, K.R.B. Singh, A.K. Yadav, V. Nayak, J. Singh, P.R. Solanki, R.P. Singh, Biosens. Bioelectron: X 11 (2022) 100153, https://doi.org/10.1016/j.biosx.2022.100153.
[7] I. Cong, S. Choi, M.D. Lukin, Nat. Phys. 15 (2019) 1273–1278, https://doi.org/10.1038/s41567-019-0648-8.
[8] X. Xu, M. Tan, B. Corcoran, J. Wu, A. Boes, T.G. Nguyen, S.T. Chu, B.E. Little, D. G. Hicks, R. Morandotti, A. Mitchell, D.J. Moss, Nature 589 (2021) 44–51, https://doi.org/10.1038/s41586-020-03063-0.
[9] Y. Li, S. Guo, B. Wang, J. Sun, L. Zhao, T. Wang, X. Yan, F. Liu, P. Sun, J. Wang, S. C. Tan, G. Lu, n/a, InfoMat (2024) e12544, https://doi.org/10.1002/inf2.12544.
[10] Y. LeCun, Y. Bengio, G. Hinton, Nature 521 (2015) 436–444, https://doi.org/10.1038/nature14539.
[11] M. Wang, T. Wang, P. Cai, X. Chen, Small Methods 3 (2019) 1900025, https://doi.org/10.1002/smtd.201900025.
[12] Y. Cheng, Y. Ma, L. Li, M. Zhu, Y. Yue, W. Liu, L. Wang, S. Jia, C. Li, T. Qi, J. Wang, Y. Gao, ACS Nano 14 (2020) 2145–2155, https://doi.org/10.1021/acsnano.9b08952.
[13] J. Park, Y. Lee, J. Hong, Y. Lee, M. Ha, Y. Jung, H. Lim, S.Y. Kim, H. Ko, ACS Nano 8 (2014) 12020–12029, https://doi.org/10.1021/nn505953t.
[14] Y. Pang, X. Xu, S. Chen, Y. Fang, X. Shi, Y. Deng, Z.-L. Wang, C. Cao, Nano Energy 96 (2022) 107137, https://doi.org/10.1016/j.nanoen.2022.107137.
[15] X. Shi, X. Fan, Y. Zhu, Y. Liu, P. Wu, R. Jiang, B. Wu, H.-A. Wu, H. Zheng, J. Wang, X. Ji, Y. Chen, J. Liang, Nat. Commun. 13 (2022) 1119, https://doi.org/10.1038/s41467-022-28760-4.
[16] Y.-C. Huang, Y. Liu, C. Ma, H.-C. Cheng, Q. He, H. Wu, C. Wang, C.-Y. Lin, Y. Huang, X. Duan, Nat. Electron. 3 (2020) 59–69, https://doi.org/10.1038/s41928-019-0356-5.
[17] T.Q. Trung, N.-E. Lee, Adv. Mater. 28 (2016) 4338–4372, https://doi.org/10.1002/adma.201504244.
[18] E.A. Lumpkin, K.L. Marshall, A.M. Nelson, J. Cell. Biol. 191 (2010) 237–248, https://doi.org/10.1083/jcb.201006074.
[19] C.S. Chen, J. Cell. Sci. 121 (2008) 3285–3292, https://doi.org/10.1242/jcs.023507.
[20] S. Zhang, Y. Deng, A. Libanori, Y. Zhou, J. Yang, T. Tat, L. Yang, W. Sun, P. Zheng, Y.-L. Zhu, J. Chen, S.C. Tan, Adv. Mater. 35 (2023) 2207916, https://doi.org/10.1002/adma.202207916.
[21] S. Zhang, M. Zhou, M. Liu, Z.H. Guo, H. Qu, W. Chen, S.C. Tan, Nat. Commun. 14 (2023) 3245, https://doi.org/10.1038/s41467-023-38269-z.
[22] S. Zhang, Y. Zhou, A. Libanori, Y. Deng, M. Liu, M. Zhou, H. Qu, X. Zhao, P. Zheng, Y.-L. Zhu, J. Chen, S.C. Tan, Nat. Electron. 6 (2023) 338–348, https://doi.org/10.1038/s41928-023-00960-w.
[23] G. Jiang, G. Wang, Y. Zhu, W. Cheng, K. Cao, G. Xu, D. Zhao, H. Yu, Research 2022 (2022) 9814767, https://doi.org/10.34133/2022/9814767.
[24] D. Kang, P.V. Pikhitsa, Y.W. Choi, C. Lee, S.S. Shin, L. Piao, B. Park, K.-Y. Suh, T.-i Kim, M. Choi, Nature 516 (2014) 222–226, https://doi.org/10.1038/nature14002.
[25] W. Zhou, P. Xiao, Y. Liang, Q. Wang, D. Liu, Q. Yang, J. Chen, Y. Nie, S.-W. Kuo, T. Chen, Adv. Funct. Mater. 31 (2021) 2105323, https://doi.org/10.1002/adfm.202105323.
[26] W. Yang, H. Liu, H. Du, M. Zhang, C. Wang, R. Yin, C. Pan, C. Liu, C. Shen, Sci. China Mater. 66 (2023) 2829–2842, https://doi.org/10.1007/s40843-022-2418-1.
[27] A. Chortos, J. Liu, Z. Bao, Nat. Mater. 15 (2016) 937–950, https://doi.org/10.1038/nmat4671.
[28] G.H. Lee, T.M. Choi, B. Kim, S.H. Han, J.M. Lee, S.-H. Kim, ACS Nano 11 (2017) 11350–11357, https://doi.org/10.1021/acsnano.7b05885.

[29] S.J. Sterbing-D'Angelo, M. Chadha, K.L. Marshall, C.F. Moss, J. Neurophysiol. 117 (2016) 705–712, https://doi.org/10.1152/jn.00261.2016.
[30] K.L. Marshall, M. Chadha, L.A. deSouza, S.J. Sterbing-D'Angelo, C.F. Moss, E. A. Lumpkin, Cell Rep. 11 (2015) 851–858, https://doi.org/10.1016/j.celrep.2015.04.001.
[31] J. Suhr, P. Victor, L. Ci, S. Sreekala, X. Zhang, O. Nalamasu, P.M. Ajayan, Nat. Nanotechnol. 2 (2007) 417–421, https://doi.org/10.1038/nnano.2007.186.
[32] X. Gui, J. Wei, K. Wang, A. Cao, H. Zhu, Y. Jia, Q. Shu, D. Wu, Adv. Mater. 22 (2010) 617–621, https://doi.org/10.1002/adma.200902986.
[33] T.A. Schaedler, A.J. Jacobsen, A. Torrents, A.E. Sorensen, J. Lian, J.R. Greer, L. Valdevit, W.B. Carter, Science 334 (2011) 962–965, https://doi.org/10.1126/science.1211649.
[34] H. Hu, Z. Zhao, W. Wan, Y. Gogotsi, J. Qiu, Adv. Mater. 25 (2013) 2219–2223, https://doi.org/10.1002/adma.201204530.
[35] L. Qiu, J.Z. Liu, S.L.Y. Chang, Y. Wu, D. Li, Nat. Commun. 3 (2012) 1241, https://doi.org/10.1038/ncomms2251.
[36] S. Barg, F.M. Perez, N. Ni, P. do Vale Pereira, R.C. Maher, E. Garcia-Tuñon, S. Eslava, S. Agnoli, C. Mattevi, E. Saiz, Nat. Commun. 5 (2014) 4328, https://doi.org/10.1038/ncomms5328.
[37] H. Sun, Z. Xu, C. Gao, Adv. Mater. 25 (2013) 2554–2560, https://doi.org/10.1002/adma.201204576.
[38] X. Wang, L.-L. Lu, Z.-L. Yu, X.-W. Xu, Y.-R. Zheng, S.-H. Yu, Angew. Chem. Int. Ed. 54 (2015) 2397–2401, https://doi.org/10.1002/anie.201410668.
[39] C. Zhu, T.Y.-J. Han, E.B. Duoss, A.M. Golobic, J.D. Kuntz, C.M. Spadaccini, M. A. Worsley, Nat. Commun. 6 (2015) 6962, https://doi.org/10.1038/ncomms7962.
[40] X. Chen, H. Liu, Y. Zheng, Y. Zhai, X. Liu, C. Liu, L. Mi, Z. Guo, C. Shen, ACS Appl. Mater. Inter. 11 (2019) 42594–42606, https://doi.org/10.1021/acsami.9b14688.
[41] H. Liu, X. Chen, Y. Zheng, D. Zhang, Y. Zhao, C. Wang, C. Pan, C. Liu, C. Shen, Adv. Funct. Mater. 31 (2021) 2008006, https://doi.org/10.1002/adfm.202008006.
[42] J. Zhai, Y. Zhang, C. Cui, A. Li, W. Wang, R. Guo, W. Qin, E. Ren, H. Xiao, M. Zhou, ACS Sustain. Chem. Eng. 9 (2021) 14029–14039, https://doi.org/10.1021/acssuschemeng.1c03068.
[43] Y. Si, X. Wang, C. Yan, L. Yang, J. Yu, B. Ding, Adv. Mater. 28 (2016) 9512–9518, https://doi.org/10.1002/adma.201603143.
[44] P. Min, X. Li, P. Liu, J. Liu, X.-Q. Jia, X.-P. Li, Z.-Z. Yu, Adv. Funct. Mater. 31 (2021) 2103703, https://doi.org/10.1002/adfm.202103703.
[45] H. Lai, H. Zhuo, Y. Hu, G. Shi, Z. Chen, L. Zhong, M. Zhang, ACS Sustain. Chem. Eng. 9 (2021) 9761–9769, https://doi.org/10.1021/acssuschemeng.1c02051.
[46] G. Li, Z. Chu, X. Gong, M. Xiao, Q. Dong, Z. Zhao, T. Hu, Y. Zhang, J. Wang, Y. Tan, Z. Jiang, Adv. Mater. Technol. 7 (2022) 2101021, https://doi.org/10.1002/admt.202101021.
[47] S. Long, Y. Feng, F. He, J. Zhao, T. Bai, H. Lin, W. Cai, C. Mao, Y. Chen, L. Gan, J. Liu, M. Ye, X. Zeng, M. Long, Nano Energy 85 (2021) 105973, https://doi.org/10.1016/j.nanoen.2021.105973.
[48] L. Pu, H. Ma, J. Dong, C. Zhang, F. Lai, G. He, P. Ma, W. Dong, Y. Huang, T. Liu, Nano Lett. 22 (2022) 4560–4568, https://doi.org/10.1021/acs.nanolett.2c01486.
[49] Z. Chen, Y. Hu, H. Zhuo, L. Liu, S. Jing, L. Zhong, X. Peng, R.-c Sun, Chem. Mater. 31 (2019) 3301–3312, https://doi.org/10.1021/acs.chemmater.9b00259.
[50] H. Kong, P. Si, M. Li, X. Qiu, J. Liu, X. Wang, Q. Wang, Y. Li, Y. Wang, Nano Lett. 22 (2022) 3266–3274, https://doi.org/10.1021/acs.nanolett.2c00168.
[51] Y. Li, J. Long, Y. Chen, Y. Huang, N. Zhao, Adv. Mater. 34 (2022) 2200517, https://doi.org/10.1002/adma.202200517.
[52] S. Zhuo, C. Song, Q. Rong, T. Zhao, M. Liu, Nat. Commun. 13 (2022) 1743, https://doi.org/10.1038/s41467-022-29424-z.
[53] Y. Yang, J. Sun, J. Wen, S. Mo, J. Wang, Z. Zhang, G. Wang, M. Liu, H. Liu, Cell Rep. Phys. Sci. 2 (2021) 100535, https://doi.org/10.1016/j.xcrp.2021.100535.

Mr Wenke Yang, currently a PhD degree candidate in National Engineering Research Center for Advanced Polymer Processing Technology at Zhengzhou University, obtained his master degree in Materials Science and Engineering at Hainan University, Haikou, China (2020). His research interests focus on multifunctional flexible wearable electronic devices.

Mr Shun Liu, currently a PhD degree candidate in National Engineering Research Center for Advanced Polymer Processing Technology at Zhengzhou University, obtained his master degree in Electronic Information at Zhengzhou University, Zhengzhou, China (2023). His research interests focus on multifunctional flexible wearable electronic devices.

Mr Ziqi Wang, currently a PhD degree candidate in National Engineering Research Center for Advanced Polymer Processing Technology at Zhengzhou University, obtained his banchelor degree in Material Science and Engineering at Zhengzhou University, Zhengzhou, China (2022). His research interests focus on multifunctional flexible composites for wearable capacitive pressure sensor.

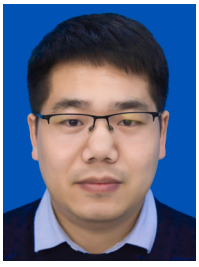

Prof. Hu Liu, currently an Associate Professor of National Engineering Research Center for Advanced Polymer Processing Technology (NERC) of Zhengzhou University, obtained his PhD from Zhengzhou University (2017), and worked as a joint PhD student with Prof. Zhanhu Guo at University of Tennessee, Knoxville, sponsored by China Scholarship Council (2015–2016). His current research interest focuses on the multifunctional polymer-based nanocomposites, especially the conductive polymer composites based sensor, electromagnetic shielding materials and thermal insulating aerogel.

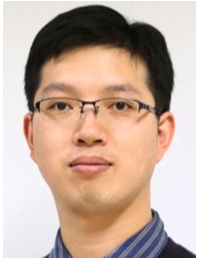

Prof. Caofeng Pan received his B.S. degree (2005) and Ph.D. degree (2010) in Materials Science and Engineering from the Tsinghua University, China. He then joined the group of Prof. Zhong Lin Wang at the Georgia Institute of Technology as a postdoctoral fellow from 2010 to 2013. He is currently the Executive Dean of the Institute of Atomic Manufacturing at the Beihang University. His research interests mainly focus on the fields of piezotronics/piezophototronics for fabricating new electronic and optoelectronic devices, nanopower source, hybrid nanogenerators, and self-powered nanosystems.

Prof. Chuntai Liu, currently a Professor of the National Engineering Research Center for Advanced Polymer Processing Technology (NERC) of Zhengzhou University, obtained his PhD from Zhengzhou University (2003), and worked as a visiting scholar at the Ohio State University (2006–2007). He serves as the deputy director of NERC of Zhengzhou University. His research focuses on multifunctional polymer composites including processing-microstructure-properties.

Prof. Changyu Shen, currently a professor of the National Engineering Research Center for Advanced Polymer Processing Technology (NERC) of Zhengzhou University and an academician of Chinese Academy of Sciences, obtained his M.S. and Ph.D. from Dalian University of Technology in 1987 and 1990 respectively. Shen has made original and innovative contributions to numerical simulation of plastic forming process, optimization design and manufacture of plastic mold as well as structured and lightweight composites. He now serves as the director of NERC of Zhengzhou University.